



Unveiling the enhancing mechanism of cycling stability of $\text{Li}_{1.2}\text{Mn}_{0.54}\text{Ni}_{0.13}\text{Co}_{0.13}\text{O}_{2-x}\text{F}_x$ cathode materials

Chen Liang^{1,2} · Panpan Zhang^{1,2} · Hui Huang^{1,2,3} · Chao Gao^{1,2,3} · Jun Guo^{1,2,3} · Yapeng He^{1,2,3}

Received: 27 December 2022 / Revised: 30 March 2023 / Accepted: 14 April 2023 / Published online: 8 May 2023
© The Author(s), under exclusive licence to Springer-Verlag GmbH Germany, part of Springer Nature 2023

Abstract

Lithium-rich manganese-based material is one of the most promising cathode materials for Li ion battery due to its low cost and high specific capacity. However, the irreversible evolution of oxygen and migration of transition metals (TM) restricts its widely practical application. In this paper, F-doped $\text{Li}_{1.2}[\text{Mn}_{0.54}\text{Ni}_{0.13}\text{Co}_{0.13}]\text{O}_2$ was prepared by co-precipitation and high temperature solid-state reaction method. The effects of F-doping on the electrochemical properties of $\text{Li}_{1.2}[\text{Mn}_{0.54}\text{Ni}_{0.13}\text{Co}_{0.13}]\text{O}_2$ during the charge–discharge procedure were investigated. Results show that $\text{Li}_{1.2}[\text{Mn}_{0.54}\text{Ni}_{0.13}\text{Co}_{0.13}]\text{O}_{1.95}\text{F}_{0.05}$ sample has the excellent cycling stability; the discharge-specific capacity reaches 182.9 mAh g^{-1} after 200 cycles, with a capacity retention rate of 87.9%, which was much higher than that of the original sample (133.2 mAh g^{-1} and 77.5%). The relevant properties proved that F-doping can inhibit the irreversible evolution of oxygen, alleviate the structural degradation of the material, and further alleviate the dissolution of transition metals by suppressing the interfacial side reactions. This result provides reference for the practical application of Li-rich cathode materials.

Keywords Lithium-ion batteries · Lithium-rich manganese-based cathode · F-doping · Cycling stability

Introduction

In recent years, to satisfy the increasing requirements of the energy storage and conversion fields, developing lithium-ion batteries (LIBs) with higher energy density is necessary [1, 2]. Compared to anode and electrolyte materials, the limited energy density and immature technology for cathode materials [3] have been considered to be the major bottleneck for upgrading the energy density of LIBs. Its limited performance stems from the low available capacities and cycling stability. Among cathode materials, lithium-rich manganese-based material ($\text{Li}_{1.2}\text{Mn}_{0.54}\text{Ni}_{0.13}\text{Co}_{0.13}\text{O}_2$, LMNC) has been considered one of the most promising cathode materials for

the next generation due to its high specific capacity (the theoretical capacity $> 250 \text{ mAh g}^{-1}$ for 1 Li^+ extraction, and about 378 mAh g^{-1} for 1.2 Li^+ extractions) [4], high energy density (about 900 Wh Kg^{-1} vs. Li metal), and low cost.

As shown in Fig. S1 [5], two plateaus corresponding to the multiple electrons redox reaction (lattice oxygen participates in charge compensation) in embedding and disembedding procedure for lithium ions were observed in the initial charge–discharge curve, leading to the high theoretical capacity of lithium-rich manganese-based cathode material. In the first stage ($< 4.5 \text{ V}$), a reversible process for Ni^{2+} and Co^{3+} ions oxidized to Ni^{4+} and Co^{4+} is occurred during lithium ions extracted from the lithium layer [6, 7]. The second stage ($\geq 4.5 \text{ V}$) stands for the activation of Li_2MnO_3 phase, accompanying with the lattice oxygen activity in form of reversible bulk oxygen redox ($\text{O}_2 \rightarrow \text{O}_n$, $n < 2$), leading to higher capacity [8]. Unfortunately, the process mentioned above is a semi-reversible reaction, part of the oxidized oxygen cannot be utilized during the following electrochemical cycles, leading to the loss of the irreversible lattice oxygen and the generation of oxygen vacancy. Meanwhile, the irreversible oxygen evolution, resulting in the removal of 2Li^+ and O^{2-} by oxygen loss following by the cationic rearrangement, leads to the phase transformation from layered

✉ Hui Huang
huihuanghan@kust.edu.cn

¹ Faculty of Metallurgical and Energy Engineering, Kunming University of Science and Technology, Kunming 650093, China

² Metallurgical Electrode Material Engineering Technology Research Center of Yunnan Province, Kunming 650106, China

³ Kunming Hendera Science and Technology Co. Ltd, Kunming 650106, China

to rock-salt or spinel-like structure and the generation of internal grain strain to cause microstructural defects, such as dislocation core and cracks [4, 9]. What's worse, the non-uniformly distributed TM elements induced by cationic rearrangement on the particle surface will trigger the consequential heterogeneous distribution of electrochemical potential, exacerbating the formation of insulated solid electrolyte interface, and induce the reduction of the average valence state of TM cations and the generation of hydrofluoric acid (HF) [10–13]. The structural collapse, poor electro-chemical performance, and low initial coulombic efficiency (ICE) of LMNC are assigned to the reasons we discussed above.

Until now, considerable doping ions, including Na^+ [14, 15], Ce^{3+} [16], Mg^{2+} [15], and F^- [17], have been tried to solve the problems mentioned above by tuning local electronic structure and coordinated environment to regulate the oxygen redox activity and improve the electrochemical properties of LMNC. In contrast with other dopant ions, F has received tremendous attention for its unique electronegativity, which can improve the cycling stability of cathode material. For instance, pieces of literature [18, 19] proved that F doping is an effective method in inhibiting the formation of SEI layers and further improving the cycling stability of lithium-rich layered materials from 72.4 to 88.1% after 50 cycles at room temperature. Most investigations were focused on improving the electrochemical performance of lithium-rich manganese-based cathode material; the enhancement mechanism of action in improving the cycling stability was little investigated, especially for lithium layer spacing and phase transition during the charge–discharge process.

F-doped LMNC samples were prepared by co-precipitation method. The effect of F^- content on the electrochemical properties of LMNC was investigated. The results exhibit that F doping is beneficial for improving the electrochemical properties of lithium-rich materials. Furthermore, the enhancement mechanism on cycling stability and discharge capacity was investigated from aspects of phase transition in charge–discharge process by means of in situ XRD; crystal structure stability by comparing the micro structure before after cycle process, and lithium ions diffusion rate by calculating the Warburg impedance coefficient.

Experimental section

Synthesis of $\text{Li}_{1.2}\text{Mn}_{0.54}\text{Ni}_{0.13}\text{Co}_{0.13}\text{O}_{2-x}\text{F}_x$ materials

The F-doped $\text{Li}_{1.20}\text{Mn}_{0.54}\text{Ni}_{0.13}\text{Co}_{0.13}\text{O}_{2-x}\text{F}_x$ (LMNC- F_x , $x=0.03, 0.05, \text{ and } 0.07$) was prepared by a co-precipitation method. Based on the stoichiometric ratio (molar ratio=0.54:0.13:0.13), 2 mol L^{-1} of $\text{MnSO}_4\cdot\text{H}_2\text{O}$, $\text{NiSO}_4\cdot 6\text{H}_2\text{O}$, and $\text{CoSO}_4\cdot 7\text{H}_2\text{O}$ and 2 mol L^{-1} of Na_2CO_3

solution were simultaneously added to the continuously stirred aqueous solution to obtain TMCO_3 (TM = Ni, Co, Mn). The pH value of the solution was controlled to 7.9 by the chelating agent $\text{NH}_3\cdot\text{H}_2\text{O}$. The obtained TMCO_3 was roasted in a tube furnace at 500 °C for 5 h, naturally cooled to room temperature, and then calcined with a mixture of lithium source- Li_2CO_3 (5% mass excess) and fluorine source-LiF (with stoichiometric amount) in a tube furnace at 900 °C for 12 h. In this case, the excess Li_2CO_3 was used to compensate for the loss of elemental lithium during the high temperature calcination. For different amounts of LiF, the synthesized samples were named LMNC- $\text{F}_{0.03}$, LMNC- $\text{F}_{0.05}$, and LMNC- $\text{F}_{0.07}$. LMNC was prepared with the same process mentioned above without adding the fluorine source.

Materials characterizations

The lattice structure of the pristine, LMNC- $\text{F}_{0.03}$, LMNC- $\text{F}_{0.05}$, and LMNC- $\text{F}_{0.07}$ samples powder is detected by X-ray diffraction (XRD, Rigaku Ultima IV, Japan) using a Cu source 40 kV, 40 mA. The content of various metal ions in the cathode samples was determined on the inductively coupled plasma-optical emission spectroscopy (ICP-OES, Prodigy, USA). The morphology and microstructure of the pristine and modified samples were observed via field-emission scanning electron microscope (FESEM, Hitachi SU8010, Japan). The element valence states and composition of those samples were characterized by X-ray photoelectron spectroscopy analyzer (XPS, Thermo Fisher, USA, Al $\text{K}\alpha$ X-ray source).

In situ XRD experiments were used to investigate the structure changes and phase transition of LMNC and LMNC- $\text{F}_{0.05}$ during charge–discharge process in a specially designed cylindrical-type cell under 0.1 C charge–discharge in the voltage ranged from 2.0 to 4.8 V. The specially designed cylindrical-type cell's composition was similar as CR2025 coin-type cells. The data was continuously recorded ranged 2θ degree from 17 to 23° with a scan-step size 0.02° during charge–discharge processes.

Electrochemical measurement

The electrochemical performances of the pristine and modified samples were evaluated via CR2025 coin cells. The coin cells were composed of Celgard 2500 separator, electrolyte with 1 M LiPF_6 in EC, EMC, and DMC (1:1:1 in volume), and a lithium foil anode and cathode electrode, where the cathode electrodes were made of LMNC- F_x , conductive carbon, and PVDF with a weight ratio of 80:10:10. The coin cells were assembled in an argon-filled glovebox with the concentrations of moisture and oxygen contents below 0.1 ppm. The battery galvanostatic charge and discharge test were carried out on the Neware test system in the voltage

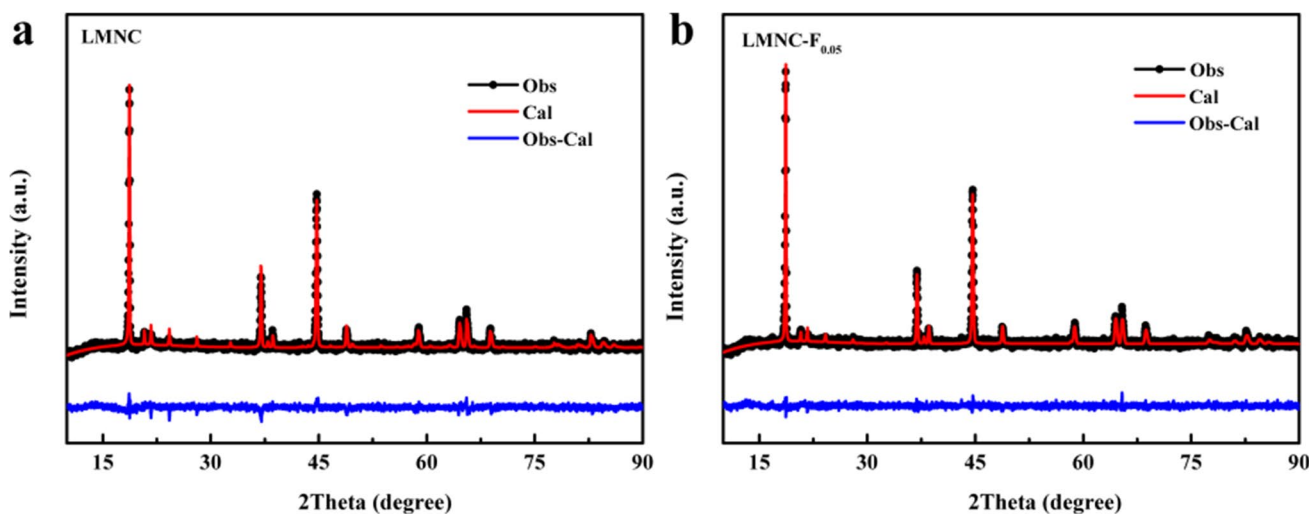


Fig. 1 XRD spectrum of **a** LMNC and **b** LMNC-F_{0.05} samples with the measurement result (black line), calculated pattern (red line), and difference curve (blue line)

range 2.0–4.8 V (vs. Li/Li⁺) at various current densities. The electrochemical impedance spectroscopy (EIS) measurement (100 kHz–0.01 Hz) was carried out on CHI760E electrochemical workstation under open circuit voltage, and the data analysis was analyzed by the ZSimDemo software.

Result and discussion

Structural characterizations and morphology

XRD patterns of LMNC and LMNC-F_x samples are shown in Fig. S2, all samples exhibit similar diffraction peaks, and the main peaks correspond to LiTMO₂ phase with the hexagonal layered structure and R-3m space group (α-NaFeO₂) based on standard PDF card PDF#87-1564. The peaks between 20 and 25° are ascribed to the Li₂MnO₃ phase (the monoclinic structure with C2/m space group) [20]. Figure S3a and b [21] show the LiTMO₂ and Li₂MnO₃ phases, respectively. For the LiTMO₂ phase, the elements in the transition metal layer are randomly distributed, whereas in the Li₂MnO₃ (i.e., Li[Li_{1/3}Mn_{2/3}]O₂) structure, Li⁺ and Mn⁴⁺ are ordered in the transition metal layer, with the Li⁺

surrounded by six Mn⁴⁺, forming a honeycomb pattern (Fig. S3c). The splitting of (006)/(102) and (018)/(110) in XRD pattern of all samples indicates the well-layered structure [22]. As previously reported, I(003)/I(104) value stands for the mixing degree of Li⁺ and Ni²⁺ in LMNC, the higher I(003)/I(104) value the lower Li⁺/Ni²⁺ mixing degree [23]. Based on the XRD pattern in Fig. S2, the I(003)/I(104) ratios of LMNC, LMNC-F_{0.03}, LMNC-F_{0.05}, and LMNC-F_{0.07} are 1.29, 1.47, 1.38, and 1.23, respectively. All of values are higher than 1.2, indicating that all samples exhibit low Li⁺/Ni²⁺ mixing degree and adequate amount of F doping is efficient in decreasing Li⁺/Ni²⁺ mixing degree. The higher Li⁺/Ni²⁺ mixing degree for the LMNC-F_{0.07} compared with other samples may be ascribed to the excessive F⁻ ions affecting the crystal structure stability of LMNC.

To further compare the difference of the crystal structure between LMNC and LMNC-F_{0.05} cathode materials, Rietveld refinements were conducted using GSAS software, the results are presented in Fig. 1 and Table 1, respectively. The reliability factors R_{wp} and R_p are both less than 10%, which verifies the reliability of the refinement results. Compared with the original sample, the lattice parameters and lattice volume of the samples are

Table 1 Cell constants, slab thickness (S), and lithium slab spacing (I) of the layered phase derived from the Rietveld refinement of the LMNC and LMNC-F_{0.05} samples

Samples	Cell constants /Å	V/Å ³	c/a	Ni/Li(3b)	z _{ox}	S _{MO2} /Å	I _{LiO2} /Å	R _w /%	R _p /%
LMNC	a=2.8470(3) c=14.2193(5)	99.814 (7)	4.994	5.7%	0.2540 (6)	2.256	2.484	3.39	2.49
LMNC-F _{0.05}	a=2.8514(4) c=14.2338(4)	100.221 (5)	4.992	3.9%	0.2572 (3)	2.167	2.577	2.81	2.22

increased after F-doping, which may be caused by the partial reduction of some TM ions due to the charge compensation mechanism. Furthermore, the slab thickness (S_{MO_2}) and lithium layer spacing (I_{LiO_2}) of the layered structure lithium-rich manganese-based materials were calculated based on the following formulas (1) and (2) [24]:

$$S_{MO_2} = \left(\frac{2}{3} - 2Z_{ox}\right)c_{hex} \quad (1)$$

$$I_{LiO_2} = \frac{c_{hex}}{3} - S_{MO_2} \quad (2)$$

where Z_{ox} is the oxygen at the 6c site and C_{hex} is the value of the lattice constant c . As presented in Table 1, the S_{MO_2} of LMNC and LMNC- $F_{0.05}$ was 2.256 Å and 2.167 Å, respectively. And the I_{LiO_2} of them was 2.484 Å and 2.577 Å, respectively. The decrease of the slab thickness S_{MO_2} can enhance the structural stability of the material, while the increase in the lithium layer spacing I_{LiO_2} is beneficial for decreasing the Li^+ diffusion energy barrier [25].

ICP and SEM with energy distribution spectra (EDS) were carried out to further prove the successfully doping

of F ion. Figure 2 shows the EDS mapping of Mn, Co, Ni, O, and F on the surface of LMNC- $F_{0.05}$, and the results indicate that all elements are uniformly distributed on the surface of the sample. The normalized ICP results were obtained and presented in Table S1 with Mn as the standardized element; the stoichiometric ratios of F elements in LMNC and LMNC- $F_{0.05}$ samples were 0 and 0.045, respectively. The results are consistent with the chemical stoichiometry as the experimental design.

XPS was carried out to investigate the effect of F doping on the valence state of transition metal elements. The XPS full spectra of LMNC further confirmed that the Mn, Co, Ni, and O elements existed in all samples, and F element was observed in the LMNC- $F_{0.05}$ samples, which is consistent with the EDS and ICP results. Figure 3b–f shows the XPS spectra of Mn 2p, Co 2p, Ni 2p, O 1s, and F 1s orbitals of LMNC and LMNC- $F_{0.05}$ samples, where the split-peak fitting was performed by XPS-peak software. As shown in Fig. 3b, the peaks with binding energies located at 642.8 eV and 654.2 eV are associated with Mn 2p_{3/2} and Mn 2p_{1/2}, respectively. The Mn 2p_{3/2} peak is divided into two characteristic peaks, where the peak with higher binding energy corresponds to Mn⁴⁺ and the peak with lower binding energy

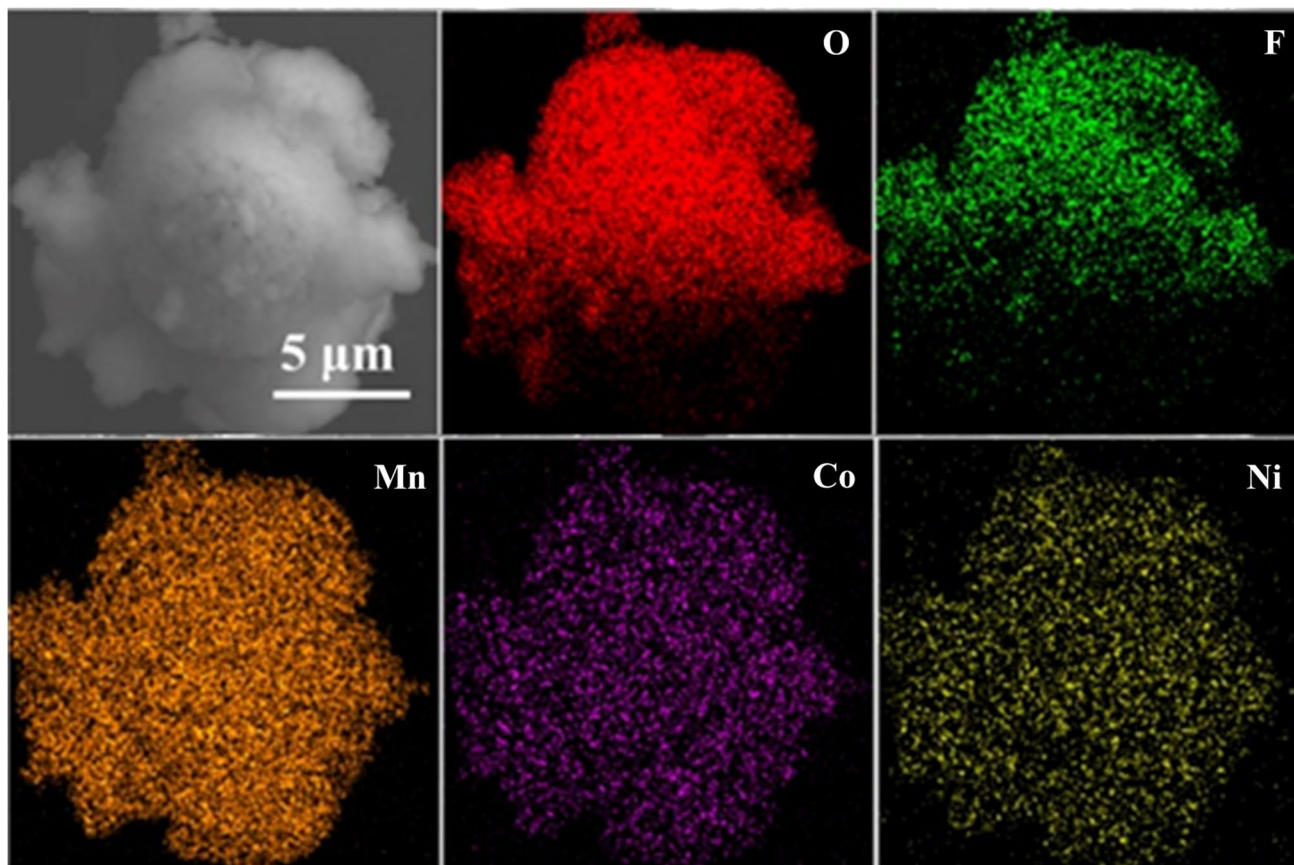


Fig. 2 The SEM and EDS images of the LMNC- $F_{0.05}$ sample

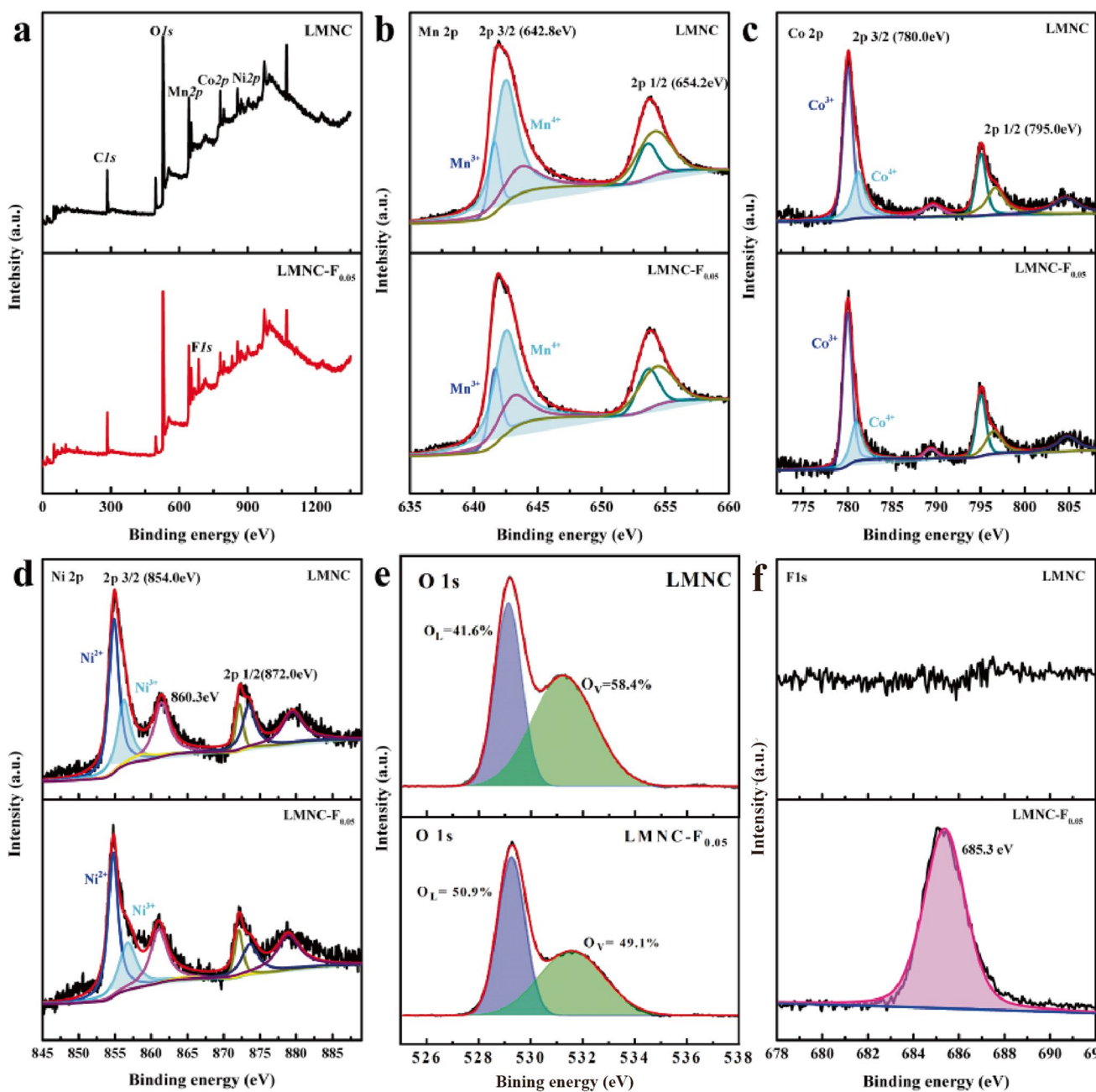


Fig. 3 a X-ray photoelectron survey spectrum of the LMNC and LMNC-F_{0.05} samples; XPS core-level spectra of **b** Mn 2p, **c** Co 2p, **d** Ni 2p, **e** O 1s, and **f** F 1s for LMNC and LMNC-F_{0.05} sample

corresponds to Mn³⁺ [26]. For the XPS spectra of Co 2p, the characteristic peaks of Co 2p_{3/2} and Co 2p_{1/2} were observed at 780 eV and 795 eV, respectively. The characteristic peak of Co 2p_{3/2} was also divided into two characteristic peaks corresponding to Co³⁺ and Co²⁺ as reported previously in the literature [27]. The peaks at 854 eV and 872 eV are ascribed to Ni 2p_{3/2} and Ni 2p_{1/2}, respectively. The peak at 860.3 eV is a satellite peak, which is responsible for the multiple splitting of the nickel oxide energy level. The fit of the Ni 2p_{3/2} spectrum can be obtained by primary peak near

854.0 eV and secondary peak at 855.5 eV, which is consistent with the standard results for Ni²⁺ and Ni³⁺ [28].

Furthermore, Mn⁴⁺ accounted for 82.6% of the total manganese and Co³⁺ for about 66.7% of the total cobalt in LMNC, while they decreased to 78.9% and 62.3% in LMNC-F_{0.05} sample, respectively. The decrease of Mn⁴⁺ and Co³⁺ ions may be ascribed to the partial reduction of Mn⁴⁺ and Co³⁺ to Mn³⁺ and Co²⁺ ions due to the substitution of O²⁻ by F⁻. The reduced TM ions (Mn³⁺, Co²⁺) have larger ionic radii, thus balancing the decrease in lattice parameters

after F^- ($r_{F^-}=1.33 \text{ \AA}$, $r_{O_2}=1.40 \text{ \AA}$) [29], and it also explains the reasons for the subtle differences in the chemical valence of TM ions (Mn^{4+}/Mn^{3+} and Co^{3+}/Co^{2+}) and the increase in lattice constants a and c in LMNC- $F_{0.05}$ sample. Based on Fig. 3e, the binding energies of 529 eV corresponding to lattice oxygen (O_L) of LMNC- $F_{0.05}$ are higher than that of LMNC, while the binding energies of 531 eV corresponding to oxygen vacancies (O_V) of LMNC- $F_{0.05}$ are lower than that of LMNC [30]. It indicates that F^- doping is effective in reducing the content of O_V , which is beneficial for reducing the diffusion of O_V during the de-lithium process, and further alleviating the structural degradation caused by TM ion migration and stabilizing the crystal structure of the material [31].

According to the results above, F ion has been successfully doped into LMNC and it is valid in tuning Li^+/Ni^{2+}

mixing degree, which may influence the electrochemical properties. Figure 4a shows the initial charge/discharge curves at 0.1C of LMNC and LMNC- F_x samples, all samples exhibit similar charge/discharge curves. The voltage plateau between 4.0 and 4.5V corresponds to the oxidation peak around 4.2 V in the dQ/dV curve (Fig. 4b), which is due to the Ni^{2+}/Co^{3+} to Ni^{4+}/Co^{4+} oxidation reaction with the simultaneous Li^+ delamination from the lithium layer of the $LiTMO_2$ phase. The platform between 4.5 and 4.8V is attributed to the activation process of Li_2MnO_3 phase accompanying with Li^+ deintercalation from both phases. As described in the introduction part, the lattice oxygen activity in form of reversible bulk oxygen redox and the evolution of lattice oxygen anions are included in this process, which corresponds to the most substantial oxidation peak at about 4.5 V in the dQ/dV curves as presented in

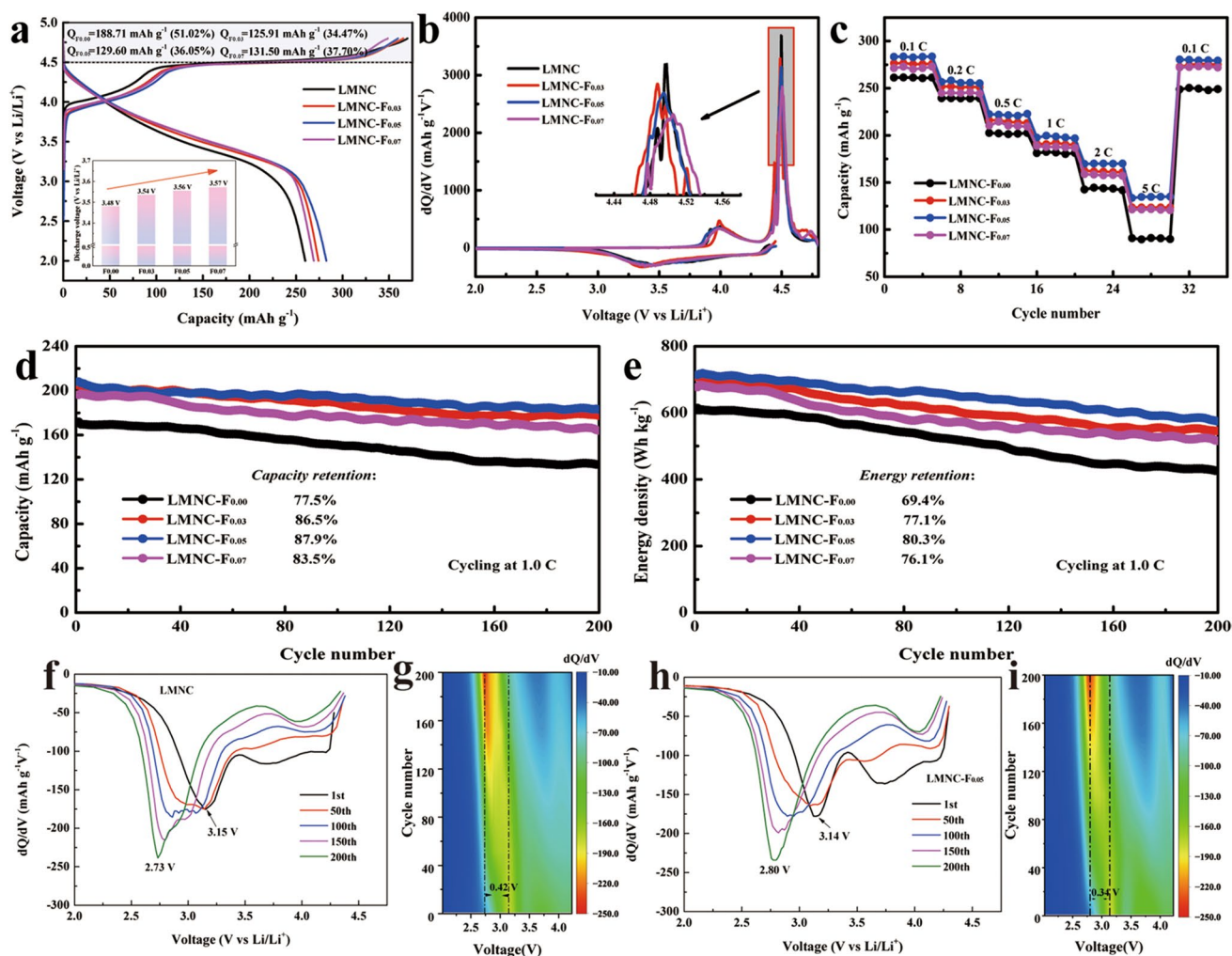


Fig. 4 a Initial charge–discharge curves at 0.1C (the inset is the median voltage of the first discharge), b the corresponding dQ/dV curves, c rate performance between 2.0 and 4.8V, d the cycling stability, and e the energy density stability during cycling of LMNC,

LMNC- $F_{0.03}$, LMNC- $F_{0.05}$, and LMNC- $F_{0.07}$ samples at 1 C; dQ/dV profiles of f LMNC and h LMNC- $F_{0.05}$. Differential discharge capacity curves of g LMNC and i LMNC- $F_{0.05}$ electrode obtained from the discharge curves during the cycling tests

Fig. 4b. Compared with LMNC, LMNC-F_x sample exhibits shorter platform between 4.5 and 4.8 V, indicating F doping is beneficial for accelerating the kinetics of the corresponding redox and suppressing the removal of 2Li⁺ and O²⁻ during initial charge process, which is conducive to improve the initial coulomb efficiencies (ICEs) (the ICEs of LMNC, LMNC-F_{0.03}, LMNC-F_{0.05}, and LMNC-F_{0.07} are 70.3%, 74.9%, 78.5%, and 77.2%, respectively) and rate capability. In addition, the initial discharge capacity and discharge voltage of LMNC-F_{0.03}, LMNC-F_{0.05}, and LMNC-F_{0.07} samples are 274.2 mAh g⁻¹ (3.54 V), 282.6 mAh g⁻¹ (3.56 V), and 270.1 mAh g⁻¹ (3.57 V), respectively. The values are much larger than that of LMNC (258.2 mAh g⁻¹ and 3.48 V), indicating the higher energy density of LMNC-F_x samples. It should be pointed out that the value of the oxidation peaks (at 3.2 V and about 4.5 V) in dQ/dV curves decreased with increasing F⁻ content, as shown in Fig. S4. The results indicate that F doping could suppress the structure transformation induced by TM migration and lattice oxygen release, and further improve crystal structure stability, and it also explains the reasons for the larger ICE of LMNC-F_x samples [32]. LMNC-F_x samples exhibit large discharge capacity under 0.1 C and larger discharge capacity under higher current density compared with LMNC, as presented in Fig. 4c, and the difference between LMNC and LMNC-F_x becomes larger with discharge rate increasing, the specific capacities are shown in Table S2. For example, the discharge capacity of LMNC-F_{0.03}, LMNC-F_{0.05}, and LMNC-F_{0.07} samples at 5C are 123.5 mAh g⁻¹, 134.7 mAh g⁻¹, and 121.5 mAh g⁻¹, respectively. The capacity values of the F-doped samples are much larger than that of LMNC (90.9 mAh g⁻¹). When the discharge rate went back to 0.1 C during the cycle process, the discharge capacity of LMNC, LMNC-F_{0.03}, LMNC-F_{0.05}, and LMNC-F_{0.07} were returned to 249.1 mAh g⁻¹ (95.4% of the corresponding initial discharge capacity), 274.8 mAh g⁻¹ (99.6%), 279.8 mAh g⁻¹ (98.7%), and 272.5 mAh g⁻¹ (100.3%), respectively, indicating F doping is conducive to improving the reversibility of LMNC during cycle process.

Cycling stability and energy density are also important indicators for the practical application of cathode material in LIBs, thus the cycling stability of LMNC and LMNC-F_x samples under 1 C was investigated and the corresponding energy density was calculated, as presented in Fig. 4d and e. The 200th discharge capacities of LMNC-F_{0.03}, LMNC-F_{0.05}, and LMNC-F_{0.07} are 177.9 mAh g⁻¹, 182.9 mAh g⁻¹, and 164.0 mAh g⁻¹ at 1 C, with high capacity retention rates of 86.5%, 87.9%, and 83.5%. The corresponding energy density is 545.5 Wh kg⁻¹, 573.7 Wh kg⁻¹, and 515.3 Wh kg⁻¹, which is higher than that of LMNC (133.2 mAh g⁻¹, 77.5%, and 425.8 Wh kg⁻¹), indicating that F doping is good for improving the cycling stability and corresponding energy density of LMNC.

As previously reported, the intensity and position of the peak in dQ/dV curve are relevant to the discharge capacity and the redox reaction potential, respectively. Thus, the superior electrochemical performance including high operating voltage, large capacity, and voltage retention of LMNC-F_{0.05} can be directly confirmed by dQ/dV curves, which were obtained from each fifty cycles during discharge process (Fig. 4f and h). The cathode peak near 3.15 V in these curves corresponds to the reduction peak of Mn⁴⁺. It should be pointed that the stronger peak of LMNC in initial cycle is mainly ascribed to the larger content of Mn⁴⁺ ions, as demonstrated in XPS results. The peak intensity of LMNC exhibits a continuous decrease during the cycle procedure and is more severe after 50 cycles. Besides, an obvious shift in the peak position of LMNC is from 3.15 to ~2.73 V after 200 cycles, implying a serious capacity decay and operating voltage attenuation, which is mainly ascribed to the serious dissolution of Mn during the cycle procedure [33], as demonstrated by the EDS results of the electrodes after the cycle process (Fig. S5). Based on the results, the transition metal atom ratio ((Mn/Co + Mn/Ni)/2) of LMNC is 3.62, much lower than that of LMNC-F_{0.05} (4.13), indicating the more serious dissolution of Mn ions on the surface of LMNC. In contrast, for LMNC-F_{0.05}, the peak position changed from 3.14 to 2.80 V after 200 cycles, indicating the superior cycling stability in terms of capacity and voltage.

Based on the rate capability, cycling performance, and dQ/dV curve, it is confirmed that F doping is an efficient strategy in improving the electrochemical property including capacity, voltage, and energy density of LMNC. The doping content of F⁻ is closely related with the electrochemical property, and the optimal F⁻ doping content is 0.05. This is mainly attributed to the fact that the introduction of F⁻ into the oxygen site results in the formation of stronger Li-F covalent bond (557 kJ mol⁻¹) compared with Li-O bond (341 kJ mol⁻¹). Moderate amount of F doping can suppress the irreversible loss of O, reducing the irreversible capacity and further enhancing the ICE of the material, while the excessive Li-F covalent bond may interfere with the embedding of Li⁺, which leads to a lower discharge capacity as demonstrated by the shorter platform between 4.5 and 4.8 V and the lower peak in dQ/dV curves. Figure 4g and i show contour plots of the LMNC and LMNC-F_{0.05} samples corresponding to the differential discharge capacity curves, respectively, with the colors relating to the height of the peaks. The regions located around 3V with more vivid colors correspond to the reduction of Mn⁴⁺. During the cycle process, the reduction of Mn⁴⁺ is often accompanied by the decay of the voltage and the change of structure [34]. Interestingly, the drastic change in the Mn⁴⁺ reduction peak in the LMNC sample occurs around the 120th turn of the cycle, while the LMNC-F_{0.05} occurs around the 140th turn,

implying that the introduction of F suppresses the phase change of LMNC.

Consistent with the charge curves, the discharge process is also composed of two stages. The first platform between 4.5 and 3.0 V in discharge curve is attributed to the reduction of Ni^{4+} to Ni^{2+} and Co^{4+} to Co^{3+} in the cathode laminar lattice, while the discharge plateau below 3.0 V is associated with the presence of spinel structure in the laminar phase, which corresponds to the transformation process of $\text{Mn}^{4+} \rightarrow \text{Mn}^{3+}$ in the spinel structure [34], indicating the capacity between 3.0 and 2.0 V can stand for the phase transformation from layered into rock-salt or spinel-like structure. Thus, the discharge capacity percentage between 3.0 and 2.0 V from 1st to 200th discharge curves under 1C was calculated, and the results are presented in Fig. 5. The discharge capacity percentage between 3.0 and 2.0 V showed a significant change with increasing cycle process. For example, the discharge capacity percentage between 3.0 and 2.0 V of LMNC increased from 24.4% for the first discharge curves

to 53.04% for the 200th cycles. The smaller discharge capacity percentage of LMNC- F_x samples, especially for LMNC- $\text{F}_{0.05}$, indicates that the appropriate amount of F^- doping is beneficial for suppressing the phase transformation from layered into rock-salt or spinel-like structure during cycle process and further enhance the structural stability of the cathode material during cycle process.

Furthermore, in situ XRD was carried out to deeply characterize the phase transformation of LMNC and LMNC- $\text{F}_{0.05}$ during initial charge–discharge process. Figure 6a and b show the in situ XRD patterns of LMNC and LMNC- $\text{F}_{0.05}$ samples, as a counter plot with intensity in color, along with the corresponding charge–discharge curve, and the peak at about 18.7° assigned to (003) reflection. To reveal the influence of F doping on structural transformation, in situ XRD measurement for the pristine LMNC and LMNC- $\text{F}_{0.05}$ sample during initial charge–discharge process was performed. As described in previous reports, during the cycle procedure, the shift of (003) plane represents the migration of the

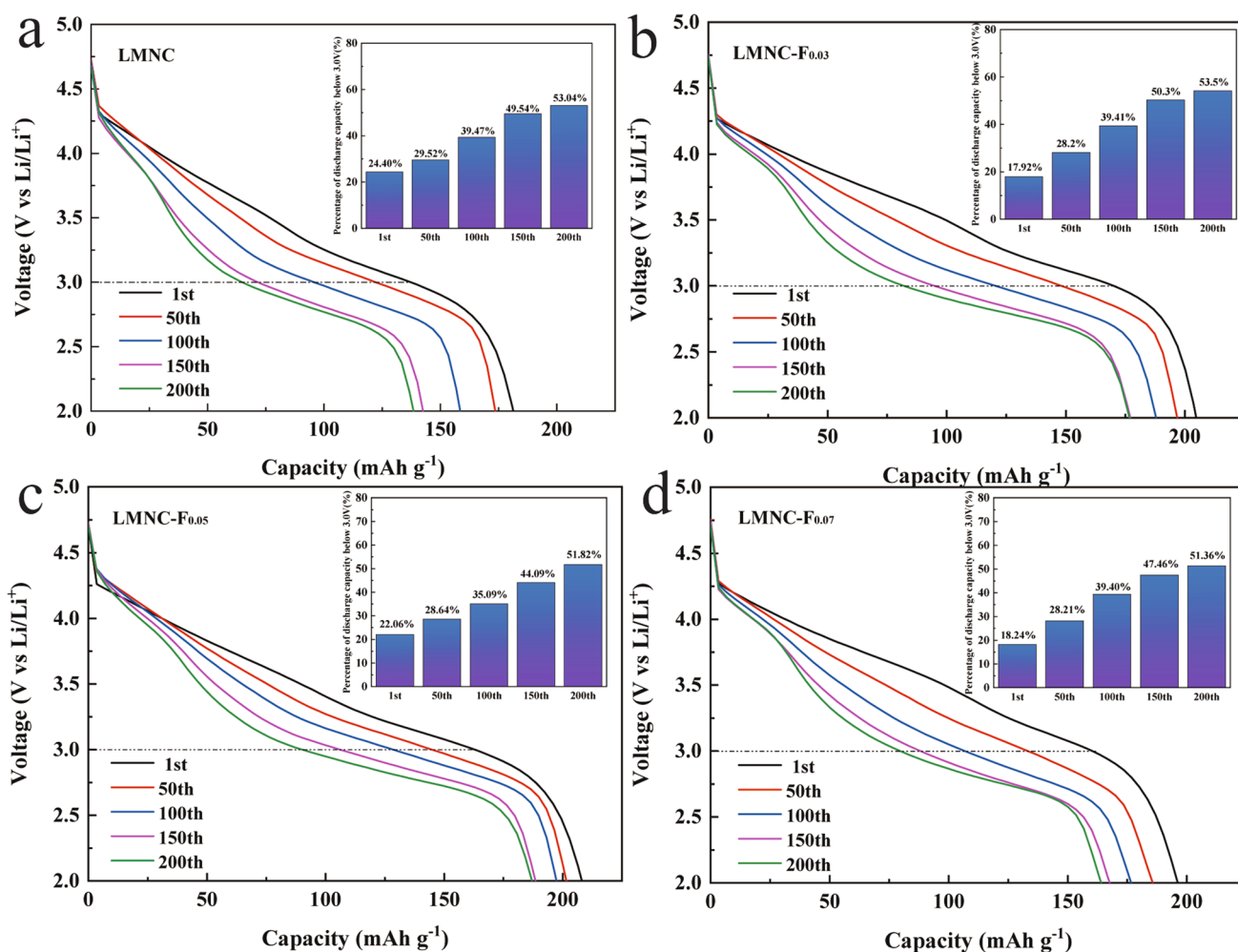


Fig. 5 a Charge–discharge profiles of LMNC, b LMNC- $\text{F}_{0.03}$, c LMNC- $\text{F}_{0.05}$, and d LMNC- $\text{F}_{0.07}$ samples during 200 cycles at 1 C

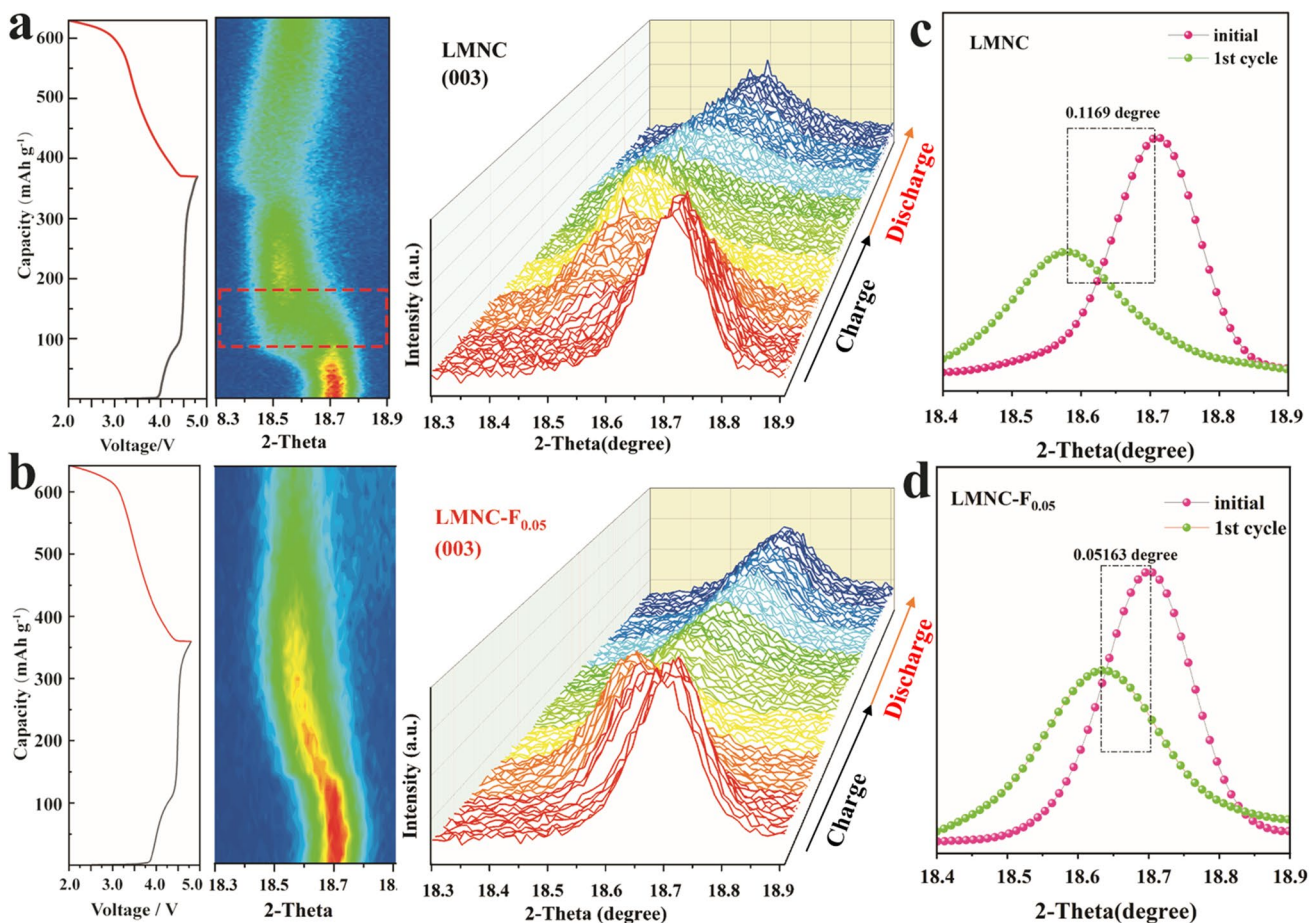


Fig. 6 In situ XRD examinations during charging/discharging of **a** LMNC and **b** LMNC-F_{0.05} in the first cycle, showing the charge/discharge curves, contour plots and XRD patterns of the 003 reflection,

and the corresponding peak shifts of the 003 reflection between fully discharged 2.0 V and the initial position during cycling of **c** LMNC and **d** LMNC-F_{0.05}

transition metal and shrinkage/elongation of c-lattice parameter [35], which also means the irreversible phase transition of LMNC [9, 36, 37]. During the first stage in charge process (< 4.5 V), the (003) peak gradually shifts to lower angle due to the increased electrostatic repulsion between adjacent oxygen layers and the continuous extraction of Li⁺ from the lithium layer [38], indicating the expansion of the lattice [9]. When charged to 4.5 V, the (003) peak shifts back to a high angle where Li⁺ ions are extracted from the transition metal layer and oxygen activation occurs for charge compensation [39]. As the voltage increased to 4.8 V, the peak shifts rapidly to a high angle; herein, the capacity is mainly derived from the activation of the Li₂MnO₃ component. As shown in Fig. 6c and d, the offset of the (003) diffraction peak is obviously reduced after F doping (0.1169° for LMNC and 0.05163° for LMNC-F_{0.05}), indicating that F doping can alleviate the lattice expansion along the c-axis direction and reduce the structural reconstruction during charge process. Upon F doping, the variation of the lattice parameters is small, indicating the internal stress of LMNC-F_{0.05} is small

during the charge–discharge process, which is beneficial for improving the crystal structure stability of LMNC. Besides, the obvious structure breakdown phenomenon is observed in the in situ XRD pattern of LMNC when charged to 4.45V, which is highlighted by the red boxes in the contour plots. This phenomenon may be induced by the phase transformation of LMNC during the charge–discharge process and it will lead to the structural instability. Interestingly, upon F doping, the LMNC-F_{0.05} reveals a smooth structural deformation during the charge process, indicating the better structural stability of LMNC-F_{0.05}, which is derived from the suppression of TM migration and lattice oxygen release. Based on the results and relevant discussion above, F doping is an efficient strategy in suppressing the phase transformation during the charge–discharge procedure, which is beneficial for improving the stability of the crystal structure.

To further investigate the action mechanism of F-doping on cycling stability, the micro structure of the electrodes of LMNC and LMNC-F_{0.05} before and after 200 cycles at 1C was investigated by SEM, and the results are presented in

Fig. 7. Both LMNC and LMNC-F_{0.05} exhibit smooth surface and complete spherical structure before cycling, and they are all composed of nano-particles. The LMNC sample was covered with a gel-like substance after the cycle process, it may be caused by the side reactions under high voltage [40]. In contrast, LMNC-F_{0.05} possesses the similar condition as before cycling. Besides, the obvious cracks were observed on the surface of the secondary particles of the LMNC sample after the cycle process, which may be induced by the larger internal grain strain originated from the phase transformation from layered into rock-salt or spinel-like structure and the larger volume change of the crystal structure with the embedding and disengaging of Li⁺ ions during charge–discharge process.

XPS analysis was performed to investigate the inhibitory effect of F-doping on side reactions of the electrode materials after the cycle process, as the results are shown in Fig. 8. According to Fig. 8a and b, two main peaks are observed in the XPS energy spectrum of F 1s. The peak near 687.7 eV is attributed to the binder PVDF or the decomposition product Li_xPO_yF_z [41], and the peak near 684.7 eV is attributed to LiF [42]. The F 1s signal intensity at 684.8 eV for the LMNC cathode after cycling was significantly higher than that of the LMNC-F_{0.05} sample, which is caused by the more side reaction products LiF which were formed on the surface of the undoped cathode. Figure 8c and d show the XPS spectra of C 1s for LMNC and LMNC-F_{0.05} electrodes

after the cycle process. The peaks at 293.1 eV, 290.5 eV, 288.5 eV, 285.7 eV, and 284.1 eV near the characteristic peaks correspond to C-C/C-H, C-O, C=O, Li₂CO₃, and C-F, respectively [43]. As shown in Fig. 8e and f, the O 1s spectrum consists of two peaks including TM-O (≈532 eV) and ROCO₂Li (≈533 eV); the peak of O_L (≈529 eV) was not detected, which is related to the release of lattice oxygen and the generation of by-products attached to the surface of the material [44, 45]. The TM-O peak of LMNC-F_{0.05} electrode is stronger than that of LMNC electrode, indicating less dissolution of TM ions [46], which is consistent with the results of the dQ/dV curve. Furthermore, the weaker ROCO₂Li peak area of LMNC-F_{0.05} electrode indicates that F-doping is also effective in suppressing the side reactions, which may be due to the enhanced stability to dehydrogenation (Fig. 8f) [47]. Based on the above results, it can be concluded that F doping plays an apparently important role in stabilizing the structure of the electrode and inhibiting the formation of CEI.

The relative intensity of the Li₂CO₃ characteristic peak in the LMNC-F_{0.05} cathode after the cycle process is lower than that of the LMNC cathode. The above result suggests that F doping can suppress the formation of interfacial by-products and alleviate the corrosion of HF generated during cycling to some extent [48]. This result explains the reasons for smooth surface, and the complete spherical structure of LMNC. It also revealed the reasons for the gel-like

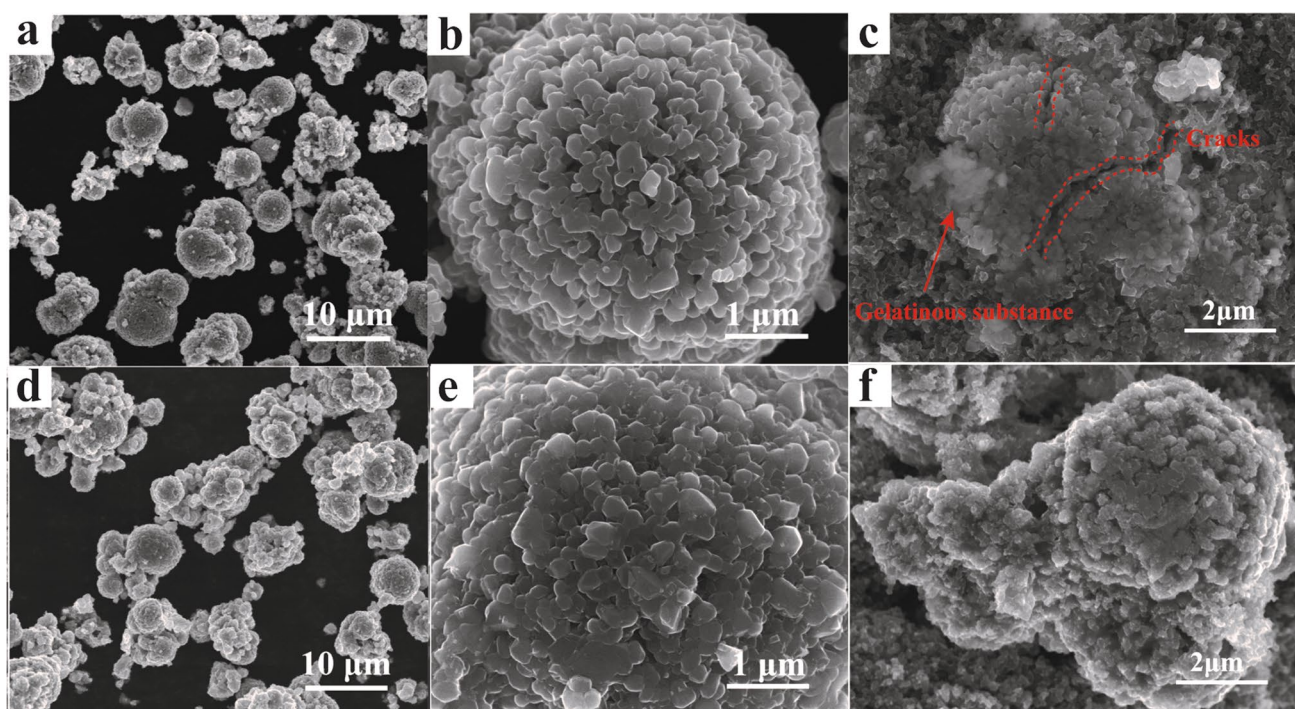


Fig. 7 **a** SEM images of LMNC before cycle process, **b** the corresponding partial enlarged image, and **c** after 200 cycles; **d** SEM images of LMNC-F_{0.05} before cycle process, **e** the corresponding partial enlarged image, and **f** after 200 cycles

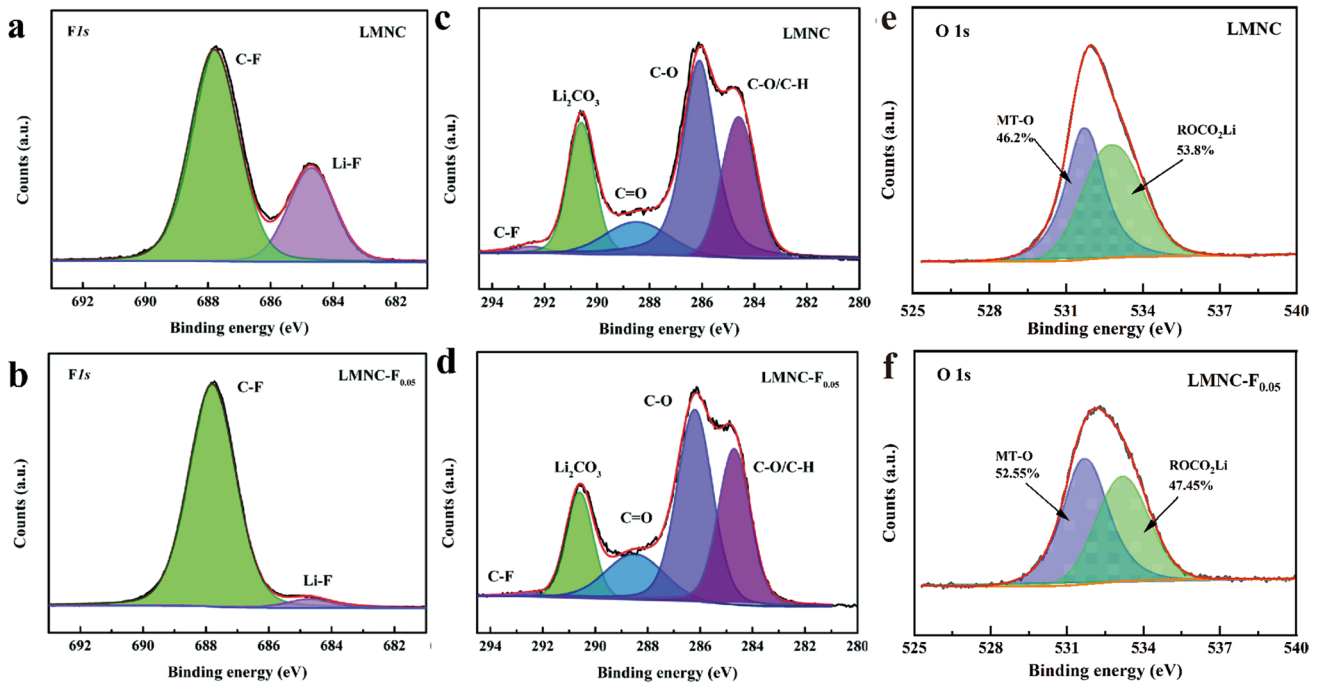


Fig. 8 XPS spectra of F 1s, C 1s, and O 1s of **a, c, and e** cycled-LMNC and **b, d, and f** cycled-LMNC-F_{0.05} electrodes

substance on the surface of LMNC after the cycle process and demonstrated by the EIS results as presented in Fig. 9. Figure 9a shows the EIS curves of LMNC, LMNC-F_{0.03}, LMNC-F_{0.05}, and LMNC-F_{0.07} samples electrodes. As can be

seen from Fig. 9, the EIS curves of all samples are consisted of a semicircular arc in the high-frequency region, a semi-circular arc in the middle frequency, and a sloping straight line in the low frequency. The semicircular arc in the high

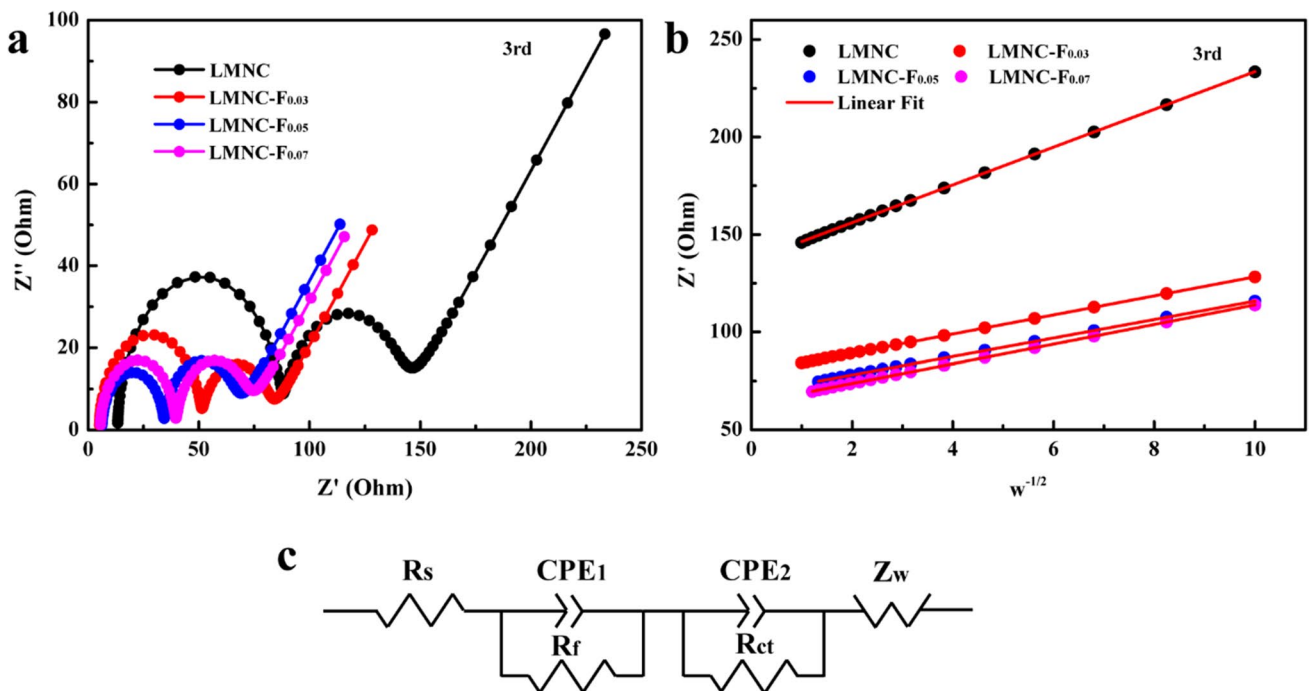


Fig. 9 **a** Nyquist plots of the LMNC, LMNC-F_{0.03}, LMNC-F_{0.05}, and LMNC-F_{0.07} samples at 0.5 C, **b** $Z''-\omega^{-1/2}$ plots for the samples in the low-frequency region obtained from EIS measurements, and **c** the equivalent circuit of the fitted impedance spectrum

frequency region is related to the cathode electrolyte interface (CEI) layer at the interface of the cathode material, the semicircular arc in the medium frequency region is related to the charge transfer resistance at the electrolyte/electrode interface, and the tilted straight line in the low frequency region corresponds to the Li^+ diffusion in the laminar lattice. Figure 9c shows the equivalent circuit diagram of the AC impedance curve, where R_s is the ohmic resistance, R_f denotes the solid electrolyte interface film resistance, R_{ct} is the charge transfer resistance at the electrode interface, and Z_w corresponds to Warburg impedance. Based on Table 2, the values of R_{ct} for LMNC, LMNC- $\text{F}_{0.03}$, LMNC- $\text{F}_{0.05}$, and LMNC- $\text{F}_{0.07}$ samples are 49.68, 34.42, 28.5, and 29.45 Ω , respectively, indicating that F doping can reduce the charge transfer resistance (R_{ct}).

According to the results mentioned above, F doping is effective in suppressing phase transformation and improving crystal structure stability, which explains the reasons for the better cycling stability of LMNC- F_x , while the larger discharge capacity and better rate performance are still unclear. Thus, the effects of F doping on the ionic diffusion coefficient (D_{Li^+}) of the LMNC and LMNC- $\text{F}_{0.05}$ samples were calculated by the equation based on Warburg diffusion [49]:

$$D_{\text{Li}^+} = 0.5 \times \left(\frac{RT}{An^2F^2C\sigma} \right)^2 \quad (3)$$

where the symbol R corresponds to the gas constant, T is the absolute temperature, A represents the area of the electrode surface, n stands for the number of transferred electrons, F represents Faraday's constant, and C is the molar concentration of Li ions. σ is the Warburg impedance coefficient, which can be obtained from the relationship between Z' and the angular frequency ($\omega^{-1/2}$) in Eq. (4) [22]:

$$Z' = R_{ct} + R_f + \sigma\omega^{-1/2} \quad (4)$$

As shown in Table 2, the D_{Li^+} of LMNC, LMNC- $\text{F}_{0.03}$, LMNC- $\text{F}_{0.05}$, and LMNC- $\text{F}_{0.07}$ samples were 4.89×10^{-13} , 1.92×10^{-12} , 2.06×10^{-12} , and 1.81×10^{-12} $\text{cm}^2 \text{ s}^{-1}$, respectively. The faster Li^+ transmission rate accounts for the larger discharge capacity of LMNC- F_x in rate and cycle process.

Table 2 Fitting results of the equivalent circuit from the Nyquist curves for all the samples and calculation results of Li^+ diffusion coefficient

Sample	R_f/Ω	R_{ct}/Ω	$\sigma/\Omega \text{ cm}^2 \cdot \text{s}^{-0.5}$	$D_{\text{Li}^+}/\text{cm}^2 \cdot \text{s}^{-1}$
LMNC	73.88	49.68	9.68	4.89×10^{-13}
LMNC- $\text{F}_{0.03}$	45.92	34.42	4.88	1.92×10^{-12}
LMNC- $\text{F}_{0.05}$	27.78	28.5	4.72	2.06×10^{-12}
LMNC- $\text{F}_{0.07}$	33.74	29.45	5.03	1.81×10^{-12}

The larger D_{Li^+} in preliminary cycles is mainly ascribed to the decreased of slab thickness S_{MO_2} as presented in the results of XRD refinement, while the larger D_{Li^+} in long cycle process is mainly ascribed the better crystal structure stability and explains the higher discharge specific capacity and rate performance of the F-doped material.

Conclusion

In this paper, LMNC- F_x was prepared by co-precipitation method with LiF as F source. The optimal F-doping content is 0.05, as demonstrated by the rate capability and cycling stability (134.7 mAh g^{-1} under the discharge capacity of 5C and 1C with capacity retention of 87.9% after 200 cycles). The optimized mechanism of cycling stability is mainly ascribed to the efficient depressant of their irreversible release of lattice oxygen upon F doping, further alleviating cation rearrangement and phase transition, and suppressing the side reactions between electrode and electrolyte and the loss of active material, leading to the better crystal structure stability. The higher discharge capacity originates from the increased lithium layer spacing and stable structure. This paper provides the reference in optimizing the discharge capacity and cycling stability of Li-rich Mn-based cathodes.

Supplementary Information The online version contains supplementary material available at <https://doi.org/10.1007/s11581-023-05003-0>.

Funding This research is funded by the Natural Science Foundation of China (No. 51504111 and 51564029), China Postdoctoral Science Foundation (2018M633418) and Analysis and Testing Foundation of Kunming University of Science and Technology (2021M20202202075).

References

- Zhang R, Huang X, Wang D, Hoang TKA, Yang Y, Duan X, Chen P, Qin LC, Wen G (2018) Single-phase mixed transition metal carbonate encapsulated by graphene: facile synthesis and improved lithium storage properties. *Adv Func Mater* 28(10):1705817
- Wang D, Qi S, Qiu Y, Zhang R, Zhang Q, Liu S, Zhang C, Chen Z, Pan H, Cao J, Wen G (2020) High-yield production of non-layered 2D carbon complexes: thickness manipulation and carbon nanotube branches for enhanced lithium storage properties. *J Energy Chem* 59:19–29
- Shi SJ, Lou ZR, Xia TF, Wang XL, Gu CD, Tu JP (2014) Hollow $\text{Li}_{1.2}\text{Mn}_{0.5}\text{Co}_{0.25}\text{Ni}_{0.05}\text{O}_2$ microcube prepared by binary template as a cathode material for lithium ion batteries. *J Power Sources* 257:198–204
- He W, Guo W, Wu H, Lin L, Liu Q, Han X, Xie Q, Liu P, Zheng H, Wang L, Yu X, Peng DL (2021) Challenges and recent advances in high capacity Li-rich cathode materials for high energy density lithium-ion batteries. *Adv Mater* 33:2005937
- Thackeray MM, Kang SH, Johnson CS, Vaughey JT, Benedek R, Hackney S (2007) Li_2MnO_3 -stabilized LiMO_2 ($M = \text{Mn, Ni, Co}$) electrodes for lithium-ion batteries. *J Mater Chem* 17:3112–3125

6. Ku K, Hong J, Kim H, Park H, Seong WM, Jung SK, Yoon G, Park KY, Kim H, Kang K (2018) Suppression of voltage decay through manganese deactivation and nickel redox buffering in high-energy layered lithium-rich electrodes. *Adv Energy Mater* 8:1800606
7. Koga H, Croguennec L, Ménétrier M, Douhil K, Belin S, Bourgeois L, Suard E, Weill F, Delmas C (2013) Reversible oxygen participation to the redox processes revealed for $\text{Li}_{1.20}\text{Mn}_{0.54}\text{Co}_{0.13}\text{Ni}_{0.13}\text{O}_2$. *J Electrochem Soc* 160:A786
8. Xu B, Fell CR, Chi M, Meng YS (2011) Identifying surface structural changes in layered Li-excess nickel manganese oxides in high voltage lithium ion batteries: a joint experimental and theoretical study. *Energy Environ Sci* 4:2223–2233
9. Lin T, Schulli TU, Hu Y, Zhu X, Gu Q, Luo B, Cowie B, Wang L (2020) Faster activation and slower capacity/voltage fading: a bifunctional urea treatment on lithium-rich cathode materials. *Adv Func Mater* 30:1909192
10. Hong J, Lim HD, Lee M, Kim SW, Kim H, Oh ST, Chung GC, Kang K (2012) Critical role of oxygen evolved from layered Li-excess metal oxides in lithium rechargeable batteries. *Chem Mater* 24:2692–2697
11. Hu E, Yu X, Lin R, Bi X, Lu J, Bak S, Nam KW, Xin HL, Jaye C, Fischer DA, Amine K, Yang XQ (2018) Evolution of redox couples in Li and Mn-rich cathode materials and mitigation of voltage fade by reducing oxygen release. *Nat Energy* 3:690–698
12. Hekmatfar M, Kazzazi A, Eshetu GG, Hasa I, Passerini S (2019) Understanding the electrode/electrolyte interface layer on the Li-rich nickel manganese cobalt layered oxide cathode by XPS. *ACS Appl Mater Interfaces* 11:43166–43179
13. Yan P, Zheng J, Chen T, Luo L, Jiang Y, Wang K, Sui M, Zhang JG, Zhang S, Wang C (2018) Coupling of electrochemically triggered thermal and mechanical effects to aggravate failure in a layered cathode. *Nat Commun* 9:1–8
14. Hu Y, Qin Z, Pei J, Cong B, Yang X, Chen G (2020) Reduced Li/Ni disorder degree of Na-doped Li-rich layered oxide for cathode material: experimental and calculations. *ChemElectroChem* 7:246–251
15. Sun YX, Zhang LJ, Dong SD, Zeng JB, Shen Y, Li X, Ren XF, Ma LX, Hai CX, Zhou Y (2022) Improving the electrochemical performances of Li-rich $\text{Li}_{1.2}\text{Ni}_{0.13}\text{Co}_{0.13}\text{Mn}_{0.54}\text{O}_2$ through cooperative doping of Na^+ and Mg^{2+} . *Electrochim Acta* 414:140169
16. Lai XW, Hu GR, Peng ZD, Cao YB, Wang WG, Du K (2022) Cerium-doped lithium-rich $\text{Li}_{1.2}\text{Mn}_{0.56}\text{Ni}_{0.11}\text{Co}_{0.13}\text{O}_2$ as cathode with high performance for lithium-ion batteries. *Ionics*:1–12
17. Huang X, Zhang Z, He J, Bai Z, Lu L, Li J (2021) Effects of chromium/fluorine co-doping on the electrochemical performance of $\text{Li}_{1.2}\text{Ni}_{0.13}\text{Co}_{0.13}\text{Mn}_{0.54}\text{O}_2$ cathode material for lithium-ion batteries. *J Mater Sci* 56:9836–9851
18. Zheng J, Wu X, Yang Y (2013) Improved electrochemical performance of $\text{Li}[\text{Li}_{0.2}\text{Mn}_{0.54}\text{Ni}_{0.13}\text{Co}_{0.13}]\text{O}_2$ cathode material by fluorine incorporation. *Electrochim Acta* 105:200–208
19. Wang B, Cui J, Li Z, Wang H, Zhang D, Wang Q, Sun H, Hu Z (2022) Surface F-doping for stable structure and high electrochemical performance of Li-rich Mn-based cathode materials. *J Alloys Comp* 929:167304
20. Guo WB, Zhang CY, Zhang YG, Lin L, He W, Xie QS, Sa BS, Wang LS, Peng DL (2021) A universal strategy toward the precise regulation of initial coulombic efficiency of Li-rich Mn-based cathode materials. *Adv Mater* 33:2103173
21. Rozier P, Tarascon JM (2015) Li-rich layered oxide cathodes for next-generation Li-ion batteries: chances and challenges. *J Electrochem Soc* 162:A2490
22. Dahiya PP, Ghanty C, Sahoo K, Basu S, Majumder SB (2018) Suppression of voltage decay and improvement in electrochemical performance by zirconium doping in Li-rich cathode materials for Li-ion batteries. *J Electrochem Soc* 165(13):A3114
23. Fell CR, Qian D, Carroll KJ, Chi M, Jones JL, Meng YS (2013) Correlation between oxygen vacancy, microstrain, and cation distribution in lithium-excess layered oxides during the first electrochemical cycle. *Chem Mater* 25:1621–1629
24. Song B, Lai MO, Lu L (2012) Influence of Ru substitution on Li-rich $0.55\text{Li}_2\text{MnO}_3 \cdot 0.45\text{LiNi}_{1/3}\text{Co}_{1/3}\text{Mn}_{1/3}\text{O}_2$ cathode for Li-ion batteries. *Electrochim Acta* 80:187–195
25. Ceder G (2010) Opportunities and challenges for first-principles materials design and applications to Li battery materials. *MRS bull* 35:693–701
26. Song B, Lai MO, Liu Z, Liu H, Lu L (2013) Graphene-based surface modification on layered Li-rich cathode for high-performance Li-ion batteries†. *J Mater Chem A* 1(34):9954–9965
27. Zou Y, Yang X, Lv C, Liu T, Xia Y, Shang L, Waterhouse GI, Yang D, Zhang T (2017) Multishelled Ni-rich $\text{Li}(\text{Ni}_x\text{Co}_y\text{Mn}_z)\text{O}_2$ hollow fibers with low cation mixing as high-performance cathode materials for Li-ion batteries. *Adv Sci* 4:1600262
28. Li L, Wang L, Zhang X, Xue Q, Wei L, Wu F, Chen R (2017) 3D reticular $\text{Li}_{1.2}\text{Ni}_{0.2}\text{Mn}_{0.6}\text{O}_2$ cathode material for lithium-ion batteries. *ACS Appl Mater Interfaces* 9:1516–1523
29. Peng Z, Mu K, Cao Y, Xu L, Du K, Hu G (2019) Enhanced electrochemical performance of layered Li-rich cathode materials for lithium ion batteries via aluminum and boron dual-doping. *Ceram Int* 45:4184–4192
30. Gao XG, Li SH, Zhang HY, Zhang S, Chang SL, Li HX, Li S, Lai YQ, Zhang Z (2022) Constructing a robust integrated surface structure for enhancing the performance of Li-rich Mn-based oxides cathodes. *Mater Today Energy* 30:101152
31. Lee S, Jin W, Kim SH, Joo SH, Nam G, Oh P, Kim KY, Kwak SK, Cho J (2019) Oxygen vacancy diffusion and condensation in lithium-ion battery cathode materials. *Angew Chem Int Edit* 58(31):10478–10485
32. Ma Q, Chen Z, Zhong S, Meng J, Lai F, Li Z, Cheng C, Zhang L, Liu T (2020) Na-substitution induced oxygen vacancy achieving high transition metal capacity in commercial Li-rich cathode. *Nano Energy* 81:105622
33. Zheng J, Gu M, Xiao J, Polzin BJ, Yan P, Chen X, Wang C, Zhang JG (2014) Functioning mechanism of AlF_3 coating on the Li and Mn-rich cathode materials. *Chem Mater* 26(22):6320–6327
34. Gu M, Belharouak I, Zheng J, Wu H, Xiao J, Genc A, Amine K, Thevuthasan S, Baer DR, Zhang J-G (2013) Formation of the spinel phase in the layered composite cathode used in Li-ion batteries. *ACS Nano* 7:760–767
35. Si M, Wang D, Zhao R, Pan D, Zhang C, Yu C, Lu X, Zhao H, Bai Y (2019) Local electric-field-driven fast Li diffusion kinetics at the piezoelectric LiTaO_3 modified Li-rich cathode-electrolyte interphase. *Adv Sci* 7(3):1902538
36. Chernyavsky V, Kim A, Koshtyal Y, Rummyantsev A, Popovich A, Maximov MY (2022) Structural features of complete and partial activation of Li-rich cathodes studied by in-situ XRD. *Electrochimica Acta* 414:140237
37. Li X, Qiao Y, Guo S, Xu Z, Zhu H, Zhang X, Yuan Y, He P, Ishida M, Zhou H (2018) Direct visualization of the reversible O^{2-}/O^- redox process in Li-rich cathode materials. *Adv Mater* 30(14):1705197
38. Zheng H, Zhang C, Zhang Y, Lin L, Liu P, Wang L, Wei Q, Lin J, Sa B, Xie Q, Peng DL (2021) Manipulating the local electronic structure in Li-rich layered cathode towards superior electrochemical performance. *Adv Func Mater* 31(30):2100783
39. Zhang XD, Shi JL, Liang JY, Yin YX, Zhang JN, Yu XQ, Guo YG (2018) Suppressing surface lattice oxygen release of Li-rich cathode materials via heterostructured spinel $\text{Li}_4\text{Mn}_5\text{O}_{12}$ coating. *Adv Mater* 30(29):1801751
40. Zhu W, Tai Z, Shu C, Chong S, Guo S, Ji L, Chen Y, Liu Y (2020) The superior electrochemical performance of a Li-rich layered

- cathode material with Li-rich spinel $\text{Li}_4\text{Mn}_5\text{O}_{12}$ and MgF_2 double surface modifications. *J Mater Chem A* 8:7991–8001
41. Wang Y, Liu F, Fan G, Qiu X, Liu J, Yan Z, Zhang K, Cheng F, Chen J (2021) Electroless formation of a fluorinated Li/Na hybrid interphase for robust lithium anodes. *J Am Chem Soc* 143:2829–2837
 42. Zheng J, Wu X, Yang Y (2013) Improved electrochemical performance of $\text{Li}[\text{Li}_{0.2}\text{Mn}_{0.54}\text{Ni}_{0.13}\text{Co}_{0.13}]\text{O}_2$ cathode material by fluorine incorporation. *Electrochimica Acta* 105:200–208
 43. Chen L, Fan X, Hu E, Ji X, Chen J, Hou S, Deng T, Li J, Su D, Yang X (2019) Achieving high energy density through increasing the output voltage: a highly reversible 5.3 V battery. *Chem* 5:896–912
 44. Chen J, Zou G, Deng W, Huang Z, Gao X, Liu C, Yin S, Liu H, Deng X, Tian Y (2020) Pseudo-bonding and electric-field harmony for Li-rich Mn-based oxide cathode. *Adv Funct Mater* 30:2004302
 45. Fan X, Hu G, Zhang B, Ou X, Zhang J, Zhao W, Jia H, Zou L, Li P, Yang Y (2020) Crack-free single-crystalline Ni-rich layered NCM cathode enable superior cycling performance of lithium-ion batteries. *Nano Energy* 70:104450
 46. Ming Y, Xiang W, Qiu L, Hua WB, Li R, Wu ZG, Xu CL, Li YC, Wang D, Chen YX (2020) Dual elements coupling effect induced modification from the surface into the bulk lattice for Ni-rich cathodes with suppressed capacity and voltage decay. *ACS Appl Mater* 12:8146–8156
 47. Kim K, Hwang D, Kim S, Park SO, Cha H, Lee YS, Cho J, Kwak SK, Choi NS (2020) Cyclic aminosilane-based additive ensuring stable electrode–electrolyte interfaces in Li-ion batteries. *Adv Energy Mater* 10:2000012
 48. He W, Qian J, Cao Y, Ai X, Yang H (2012) Improved electrochemical performances of nanocrystalline $\text{Li}[\text{Li}_{0.2}\text{Mn}_{0.54}\text{Ni}_{0.13}\text{Co}_{0.13}]\text{O}_2$ cathode material for Li-ion batteries. *RSC Adv* 2:3423–3429
 49. Wu B, Yang X, Jiang X, Zhang Y, Shu H, Gao P, Liu L, Wang X (2018) Synchronous tailoring surface structure and chemical composition of Li-rich-layered oxide for high-energy lithium-ion batteries. *Adv Func Mater* 28:1803392

Publisher's note Springer Nature remains neutral with regard to jurisdictional claims in published maps and institutional affiliations.

Springer Nature or its licensor (e.g. a society or other partner) holds exclusive rights to this article under a publishing agreement with the author(s) or other rightsholder(s); author self-archiving of the accepted manuscript version of this article is solely governed by the terms of such publishing agreement and applicable law.